



HAL
open science

Fretting tests for cyclic plastic law identification: Application to a 1XXX aluminium crossed wire contact

Pierre Arnaud, Vincent Maurel, Siegfried Fouvry, J. Said, C. Yang, F. Hafid

► **To cite this version:**

Pierre Arnaud, Vincent Maurel, Siegfried Fouvry, J. Said, C. Yang, et al.. Fretting tests for cyclic plastic law identification: Application to a 1XXX aluminium crossed wire contact. *Tribology International*, 2023, 177, pp.107958. 10.1016/j.triboint.2022.107958 . hal-03875052

HAL Id: hal-03875052

<https://hal.science/hal-03875052>

Submitted on 28 Nov 2022

HAL is a multi-disciplinary open access archive for the deposit and dissemination of scientific research documents, whether they are published or not. The documents may come from teaching and research institutions in France or abroad, or from public or private research centers.

L'archive ouverte pluridisciplinaire **HAL**, est destinée au dépôt et à la diffusion de documents scientifiques de niveau recherche, publiés ou non, émanant des établissements d'enseignement et de recherche français ou étrangers, des laboratoires publics ou privés.

Fretting tests for cyclic plastic law identification: application to a 1XXX aluminium crossed wire contact

P. Arnaud¹, V. Maurel¹, S. Fouvry², J. Said³, C. Yang³, F. Hafid³

¹ MinesParis, PSL University, Centre for material sciences (MAT), UMR 7633 CNRS, 91003 Evry, France

² Ecole Centrale de Lyon, LTDS Laboratory, 36 av Guy de Collongue, 69130 Ecully, France

³ RTE – Direction de la R&D – Pôle Smartlab, 92073, Paris la Defense Cedex, France

Abstract

To predict the fretting fatigue endurance, it is essential to precisely evaluate the contact size extension to achieve reliable fatigue stress computations. This aspect is widely investigated in the literature regarding surface wear extension induced by gross slip slidings. It can also be critical under partial slip when significant plastic deformations are generated in the interface. A coupled approach involving a 1XXX aluminum crossed wires contact for overhead conductor application is here considered. An original Levenberg-Marquardt strategy for identifying plastic law combining cyclic tensile tests and a set of fretting scars is introduced. This new approach improves by more than 15% the contact size extension prediction of fretting and fretting-fatigue conditions compared to the usual tensile test identification strategy.

Key words: fretting, contact size, cyclic plastic properties, overhead conductor.

1. Introduction

The lifetime assessment of overhead conductors is a key point for any Transmission System Operator (TSO) in charge of an electrical power grid [1, 2]. In order to adapt interval for inspection in maintenance program and repair protocols, damage tolerance analysis is needed to assess the remaining potential of systems involved in power lines with physical comprehension. Among all the damaging loadings that affect the total lifetime of a conductor, in contact areas between wires

composing the conductor, the association of clamping force and oscillating bending movement promotes fretting fatigue [3]. Fretting loading will induce crack initiation and as soon as a microcrack exists, fatigue loading may drive the crack growth until failure [4]. Fretting is a contact load characterized by small oscillatory displacement always inferior to the contact size occurring in many industrial fields. For very severe plastic loadings and/or soft materials the extension of fretted contact area decreasing stress and local loading, is an essential aspect to predict the fretting fatigue endurance [5, 6]. Under gross slip, it is well known that surface wear plays a dominant effect in increasing contact area [7, 8]. Under partial slip, wear is not activated; however, cumulated plasticity can also induce large extension of the contact area depending on contact conditions [9].

Ambrico and Begley [10,11] first proposed loading maps describing the cyclic elastoplastic response of 2D cylinder/plane interfaces enduring fretting stressing. Following this primary work, various studies focusing on the coefficient of friction effect or plastic deformations and shakedown rate have been undertaken [12-14]. However, all these works were carried out on simplified 2D contacts considering plastic identification for independent cyclic tensile tests or oversimplified material behaviors which are not representative of real experimental cases.

The aim of this study is to improve both experimental characterization and associated mechanical behavior model in the domain of plastic properties of the aluminum used for Aluminum Steel Reinforced Conductors ACSR (fig. 1). After a brief microstructural analysis of the studied aluminum alloy, uniaxial cyclic loading tests series is detailed. From this investigation a first set of elastoplastic parameters, combining non-linear isotropic and kinematic hardening based on a standard Chaboche's law has been identified. Using this first identification of elastoplastic behavior, plastic fretting fatigue scars have been evaluated by FEA. A significant discrepancy between the modeled straining and the experiments suggests that the high compressive hydrostatic stresses observed in contact should be accounted for in the identification test series, which is not the case considering only conventional tensile test identification procedure. The identification method has been then

improved by incorporating an experimental fretting test in an optimization loop by finite element (FE) simulations. A new set of Chaboche's elastoplastic law parameters has been then identified.

Using the updated plastic law, an extensive analysis of various plain fretting and fretting fatigue scars in partial slip is performed. Final comparisons between experiments and simulations demonstrate the improvement of fretting fatigue contact size and cracking assessment, by robust plastic law identification incorporating tribological tests.

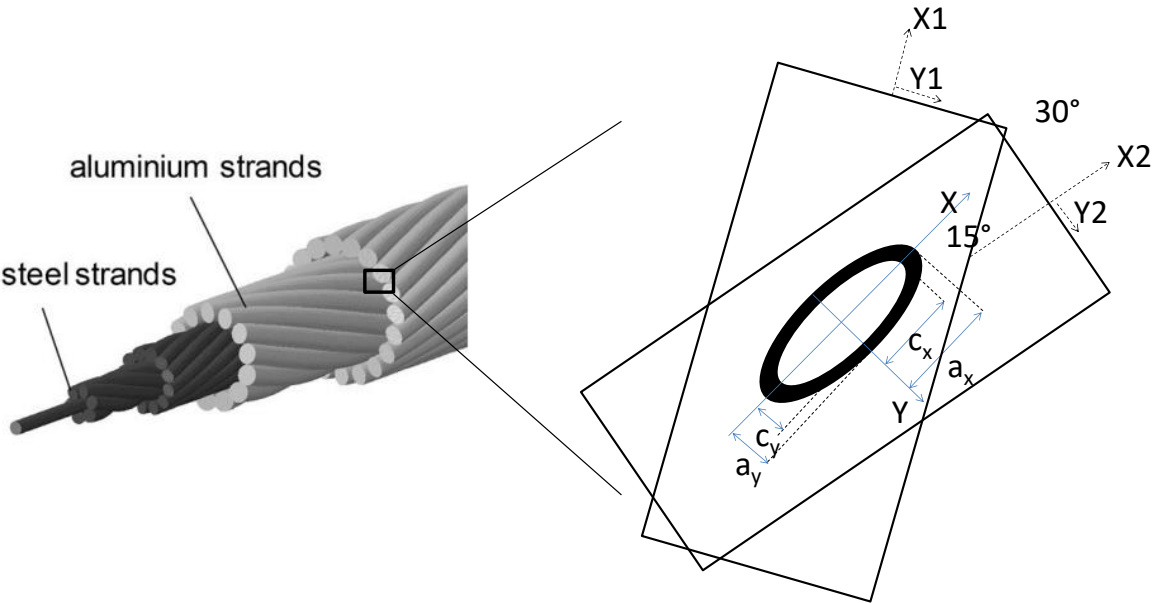


Figure 1: conductor structure and generated elliptical contact between wires

2. Materials

2.1. Aluminum wire from drawing process

The studied material consists of a quasi-pure aluminum with composition up to 99% Al. This composition was chosen to optimize the electrical condition which in turn promotes very weak mechanical properties [15]. This aluminum was casted, then rolled to give the shape of a bar. After this operation, the wires are driven through successive drawing dies of decreasing diameters, to progressively reduce the diameter of the wire to the targeted final size. The current study focuses on

specific conductor geometry with diameter, φ , of 3.6 mm. Due to the overlap angles between aluminum strands, the resulting configuration leads to a crossed cylinder contact with a total relative angle β of 30° (fig. 1). All samples used for the experimental tests were taken from a dedicated coil of aluminum strands without their helical shape in order to avoid successive manual handlings. This manipulation would have induced additional plastic deformation and residual stresses in the strands and would have impacted the mechanical properties.

2.2. EBSD analysis

In the literature, the texturing of aluminum has shown to be able to influence the properties of the wire [16]. Thus, electron backscatter diffraction (EBSD) analyses were achieved to characterize the studied face centered cubic material. Two surfaces were investigated, a first one corresponding to a normal parallel to the drawing axis direction (resp. cross-section orthogonal to the drawing axis) and a second perpendicular to this latter (resp. cross-section parallel to the drawing axis), figure 2. The normal direction of these surfaces is labeled as (001) by convention.

EBSD analyses were performed on a Thermofisher Nova scanning electronic microscope (SEM), using a step of $0.1 \mu\text{m}$ over a $100 \mu\text{m}$ square scanning area. Figure 2 displays the EBSD axial and transverse surface analysis by both inverse pole figure (IPF) and pole figure (PF). Due to the drawing process, the grains exhibit a needle-like shape which is estimated at $2 \mu\text{m}$ in diameter and several tens of microns in length. Thus, an analysis in the orthogonal plane of the drawing direction (axial) suggests a 800 grains mapping analysis. The transverse direction is not representative of the global microstructure of the considered material due to a relatively small number of grains but will allow a validation of the axial analysis.

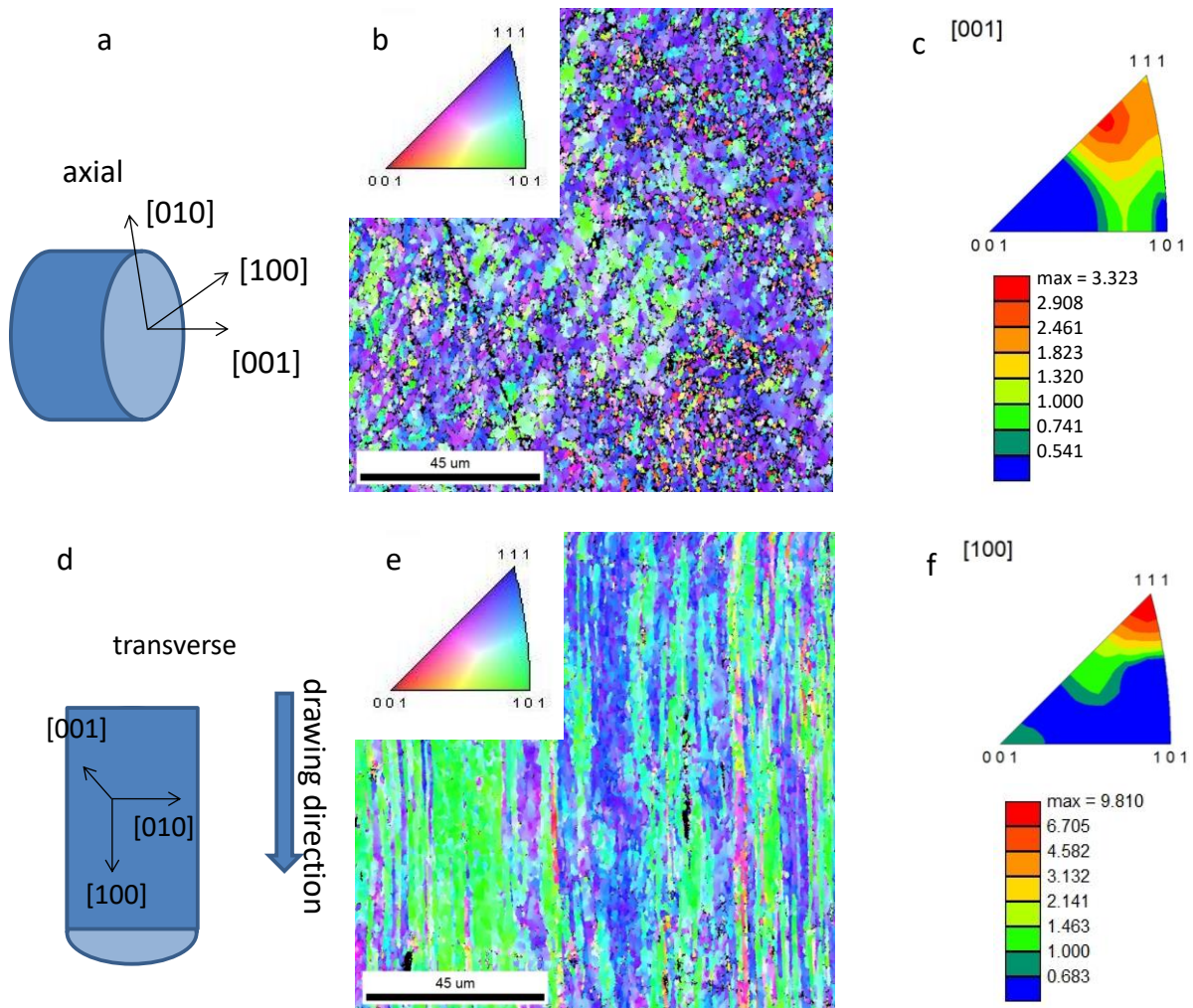


Figure 2: EBSD analysis of the studied Al-strand; (a) orientation analysis, (b) Inverse pole figure (IPF) and (c) poles figures (PF) in the drawing direction; (d) orientation analysis (e) IPF and (f) PF orthogonally to the drawing direction.

As expected, the crystalline orientation in the [001] plane corresponds to the drawing direction. A weak orientation is however observed, not exceeding index 3.3 on the scale. The $\langle 111 \rangle$ orientation in the [001] plane, defined as the preferential orientation in the sequel displays a slight misorientation in the $\langle 001 \rangle$ direction [17]. This could be attributed to recrystallization during the drawing process, corroborating literature results [18,19]. The two other planes [100] and [010] show two different orientations. These orientations are not justified by the wire manufacturing processes and remain present with low intensities. The analysis in the transverse direction presents similarity to the axial analysis: a weak orientation in $\langle 111 \rangle$ direction parallel to the direction of the wire drawing and no other preferential orientation are observed.

The misorientation analysis within a grain suggests large area axial surface with no significant deformation, whereas transverse surface displays less than half of the area with more than 5% deformation (table 1). These observations are consistent with the weak orientation observed with axial IPF and suggest that recrystallization has occurred during the drawing process. The crystal orientation is *a priori* not sufficient to influence the orthotropy of the mechanical properties for high purity aluminum alloy, so an isotropic mechanical behavior will be assumed herein.

Table 1: grain orientation spread synthesis of the axial and transversal surface analysis

Orientation spread angle	Fraction for axial analysis	Fraction for transversal analysis
0 to 1°	0.260	0.089
1 to 2°	0.121	0.08
2 to 5°	0.282	0.297

3. Identification of mechanical behavior based on uniaxial test condition

3.1. Uniaxial cyclic tensile test analysis

Cyclic tensile tests were performed on a MTS device using a 2kN cell force on aluminum wires. First two monotonic tests were performed using digital image correlation (DIC) technique so as to validate homogeneous straining of the wire before strain localization. The sample is cylindrical with a diameter of 3.6 mm and 70 mm gauge length. V shaped grips with a thin layer of rubber was used to limit necking in the grips. The behavior presents a classical evolution: initial linear elasticity is observed and then plasticity occurs. Due to the shape of the sample, the necking appeared close to the grips for the first sample but the second test shows a necking within the gage length. For both tests, the necking occurred just above 1% of longitudinal strain and for stresses around 190 MPa (fig. 3).

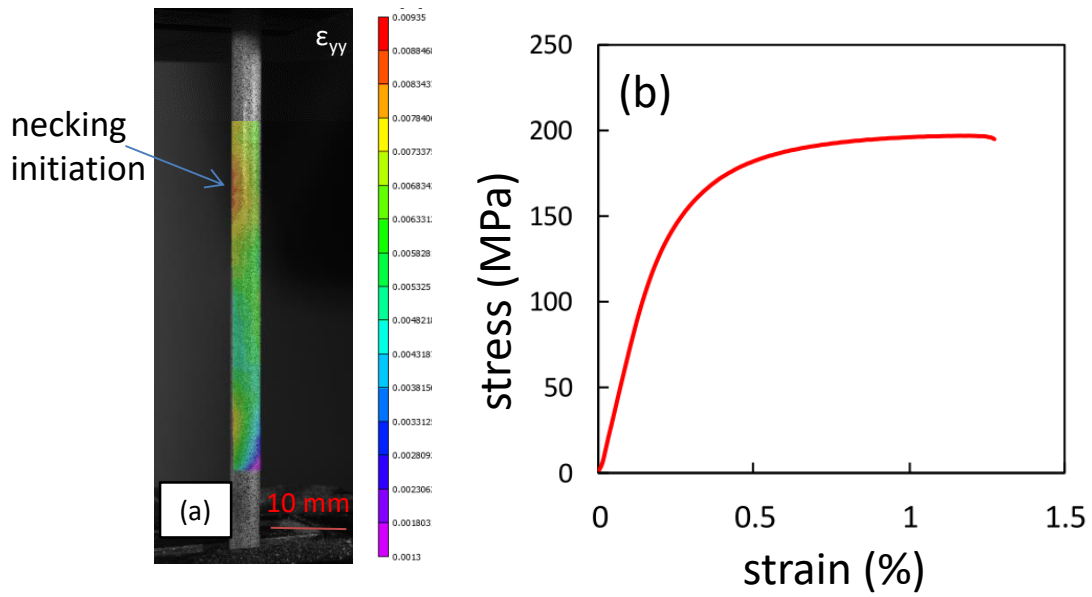


Figure 3: a) DIC of tensile test; b) stress/strain curve of the tensile test up to necking.

To characterize cyclic properties, in both tensile and compression, a shorter specimen is used: a cylindrical gauge of 3.6 mm in diameter and 10 mm in length, allow to avoid buckling. A tube with an inner diameter of 3.6 mm and an outer diameter of 5 mm over a length of 10 is used to create an extra thickness at the bases of the samples and thus better distribute the stress to once again avoid necking in the grips. The DIC and the extensometer measurement could not be performed on the samples because the spacing between the grips was too small. Thus, the displacement measured by LVDT was used and corrected by removing the deformation of the device measured without sample ($\Delta_{L,specimen} = \Delta_{L, LVDT} - \Delta_{L, actuator}$). The test series were displacement controlled using a progressive sinusoidal loading up to the targeted displacement. A total of 100 cycles have been completed. Table 2 details the testing conditions.

Table 2: conditions of uniaxial tension compression test series

test	1	2	3
mean strain	0 %	0 %	0.75 %
strain amplitude	+/- 0.45%	+/- 0.75%	+/- 0.3%

Figure 4 shows the stress-strain curves of the three tests performed, stress corresponds to the ratio F/S , S being the nominal section of the strand, and strain corresponds to the ratio of the elongation over the initial length, which remains valid for small applied strains. The tests show a significant stress-strain hysteresis characteristic of a plastic dissipation. Isotropic and kinematic hardenings are also evidenced by these tests.

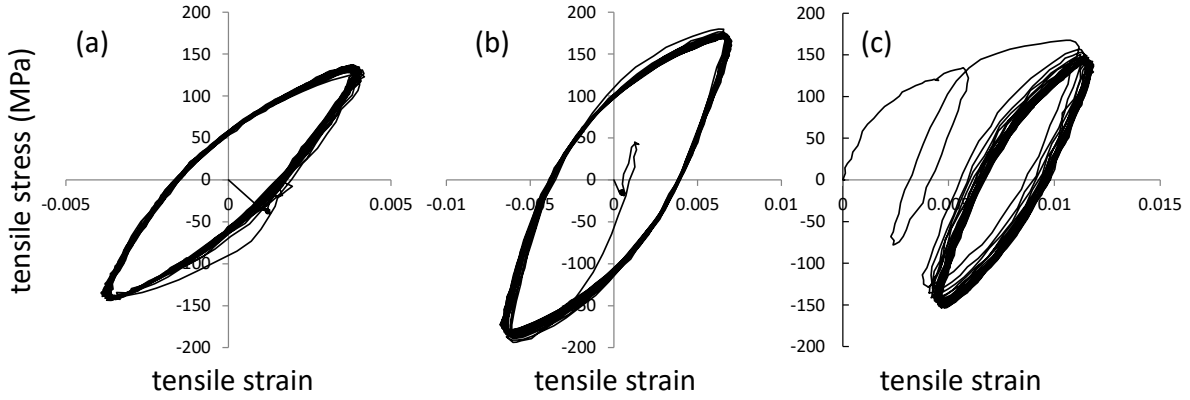


Figure 4: Experimental mechanical behavior for uniaxial testing; (a) test #1 $\Delta \epsilon = 0.45\%$; $\epsilon_{\text{mean}} = 0\%$
 (b) test #2 $\Delta \epsilon = 0.75\%$; $\epsilon_{\text{mean}} = 0\%$ (c) test #3 $\Delta \epsilon = 0.5\%$; $\epsilon_{\text{mean}} = 0.75\%$, 100 cycles.

3.2. Elastoplastic model

The chosen plastic law to reflect the studied aluminum behavior combines nonlinear isotropic and kinematic strain hardening, whose flow function f is expressed in the following equation according to the Von Mises Chaboche formalism [20]:

$$f(\underline{\underline{\sigma}}) = J(\underline{\underline{\sigma}} - \underline{\underline{X}}) - R_0 - R(p) \quad (1)$$

where $\underline{\underline{X}}$ and R correspond to the kinematic tensor and isotropic strain hardening, respectively, R_0 is the proportionality limit, and p the plastic multiplier. Hardenings are assessed through partial differential equations as follows:

$$\dot{\underline{\underline{X}}} = \frac{2}{3} C \dot{\underline{\underline{\epsilon}}}_p - D \underline{\underline{X}} \quad (2)$$

$$\text{and } \dot{R} = b(Q - R)\dot{p} \quad \text{with} \quad R = Q(1 - \exp(-bp)) \quad (3)$$

where $\underline{\dot{\epsilon}}_p$ is the plastic flow rate. For sake of simplicity, a single backstress term is used, the law being thus defined with 5 material parameters to be identified: R_0 , C, D, Q, and b.

3.3. Optimization of plastic parameters through uniaxial tensile tests (EP1)

The optimization of plastic properties is achieved by Zopt which is a tool of the Zset suite [21]. This tool is based on the Levenberg-Marquardt (L-M) algorithm which allows the user to optimize parameters by minimizing a cost function based on a residue. This residue corresponds to a quadratic difference between experimental and simulated values [22].

The model used for the simulation of the plastic properties in tension-compression will be based on a simplified FE model, represented by a single linear element with unitary sides and the loading directly applied and measured at nodes. The residue which must be minimized for tensile test is the difference between the experimental and simulated stress-strain curves, namely the tests being strain controlled, the residue is based on the evolution of modeled stress as a function of time.

A previous study of the same material indicates a 65 GPa elastic modulus and a 0.35 Poisson's coefficient [3]. Thus, to reduce the computation time, these values are prescribed to the proposed model. Therefore, only R_0 , C, D, Q and b parameters need to be identified. The optimum parameters deduced from the L-M analysis of tensile tests, so called EP1, are compiled in table 3.

Table 3: obtained set of plastic parameters by the optimization based only on tensile tests EP1, tensile and fretting tests EP2, and tensile and indentation tests EP3

Parameters	C (MPa)	D (s ⁻¹)	b (MPa)	Q	R ₀ (MPa)
EP1	51660	534	1.5	70	75
EP2	54300	575	3	68	fixed
EP3	44000	460	13	60	fixed

Figure 5 presents the comparison of stress/strain curves between experimental and EP1 model deduced from optimization. A rather good correlation is observed. We can witness a slight overestimation of the maximum stress value for each cycle for tests #1 and a slight underestimation for test #2 and #3. It is worth noting that the isotropic hardening is of a low value with a saturation b parameter of 1.5 MPa.

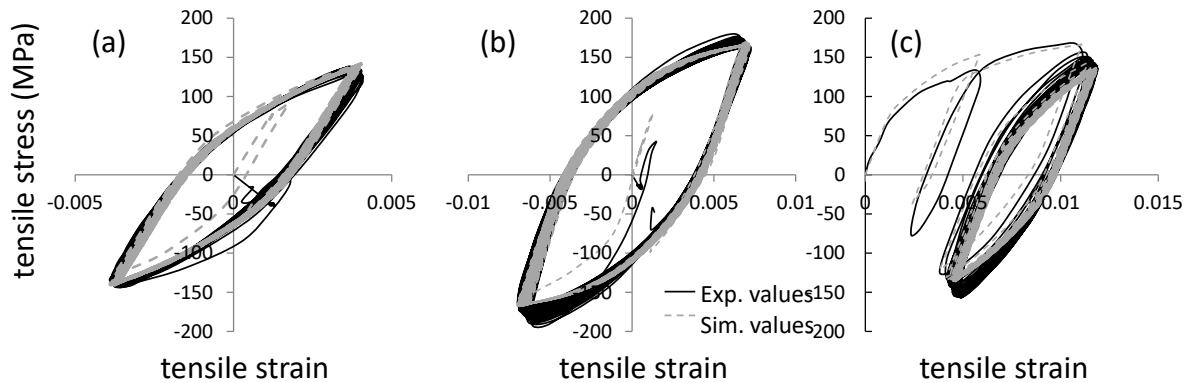


Figure 5: comparison between experimental and simulated stress/strain curves of tensile tests; (a) test #1, (b) test #2, (c) test #3.

4. Experimental plain fretting and fretting fatigue tests

The first objective of the fretting tests is to define a loading to validate the modeled mechanical behavior as described above. However, these tests could also highlight the behavior of the material with respect to fretting tests and will also provide additional information for identification optimization accounting for multiaxial loading, cyclic loading, and large strain amplitude.

4.1. Experimental set up

The plain fretting and fretting fatigue tests were carried out on the same MTS device displayed in figure 6. The 3.6 mm diameter samples are placed so as to form a 30° angle, consistently with Figure 1(b), the normal force is applied with a screw-spring system, never exceeding the targeted force and with a counter body to keep the middle wire aligned with the sensor 1 and the sensor 2. As represented in Fig. 6, the fretting fatigue experimental tests use two hydraulic actuators, a first one is

used to apply a fatigue loading on the fatigue sample, and a second one is used to drive displacement on the fretting samples, in order to induce fretting at the contact.

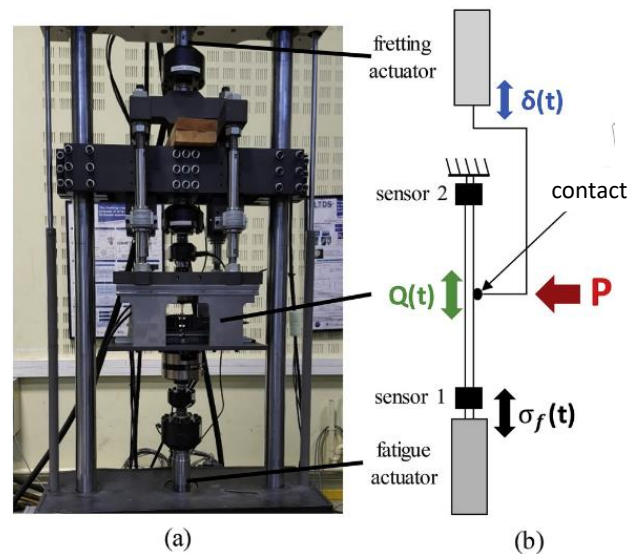


Figure 6: a) Double actuator device used for fretting fatigue mono-contact tests; b) schematic drawing of the double actuator device [8].

The targeted loading conditions aim to establish the plastic plain fretting and fretting fatigue scars under pure partial slip conditions. Therefore, the applied displacement δ^* was systematically prescribed below the gross slip regime transition δ_t^* with $Q_t^* = \mu_t P$. However, due to surface oxides and contaminations, the initial sliding coefficient μ_t is usually very low, of about 0.2, inducing a gross slip period until that coefficient of friction increases up to a sufficient value so as to shift the interface toward a steady state partial slip condition.

During this gross slip period, surface wear can be generated decaying the fretting scar geometry. To avoid this gross slip period, an increasing displacement amplitude ramp is applied so that the targeted tangential force Q^* is achieved without inducing any gross slip sliding (fig. 7). Once the tangential force is reached, 100 additional fretting cycles were performed to stabilize the plastic contact size. It is interesting to note that despite the fact that the total slip is not activated, a $(Q-\delta)$ hysteresis is still observed at the targeted partial slip tangential load ($Q=150$ N). We are going to

demonstrate later in the discussion that this typical response is induced by a plastic accommodation of the interface.

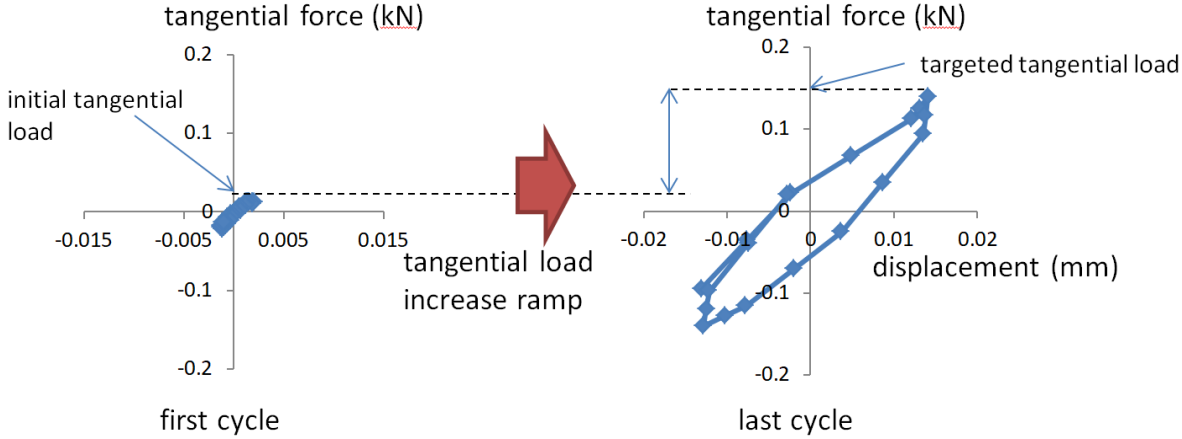


Figure 7: fretting cycles showing the applied progressive tangential loading of the contact to avoid activating transient gross slip before reaching the steady state partial slip condition ($P=200$, $Q=15$ N and $Q=150$ N).

The test loading conditions are illustrated in figure 8 and detailed in table 4. Each loading condition was repeated 3 times to obtain a representative average response of the measurements. Regarding plain fretting conditions (i.e. $\sigma_{fat}=0$ MPa), 3 levels of normal force have been applied and for each of them 3 levels of partial slip tangential forces have been considered. The effect of fatigue stress was investigated by keeping constant $P=150$ N and $Q/P=0.6$ and varying σ_{max} from 25 to 125 MPa with $R= \sigma_{min}/\sigma_{max}=0.5$. Then a crossed Q and P analysis was achieved for $\sigma_{max} = 50$ MPa. Finally, 18 different test conditions have been investigated involving more than 54 tests (fig. 8, table 4).

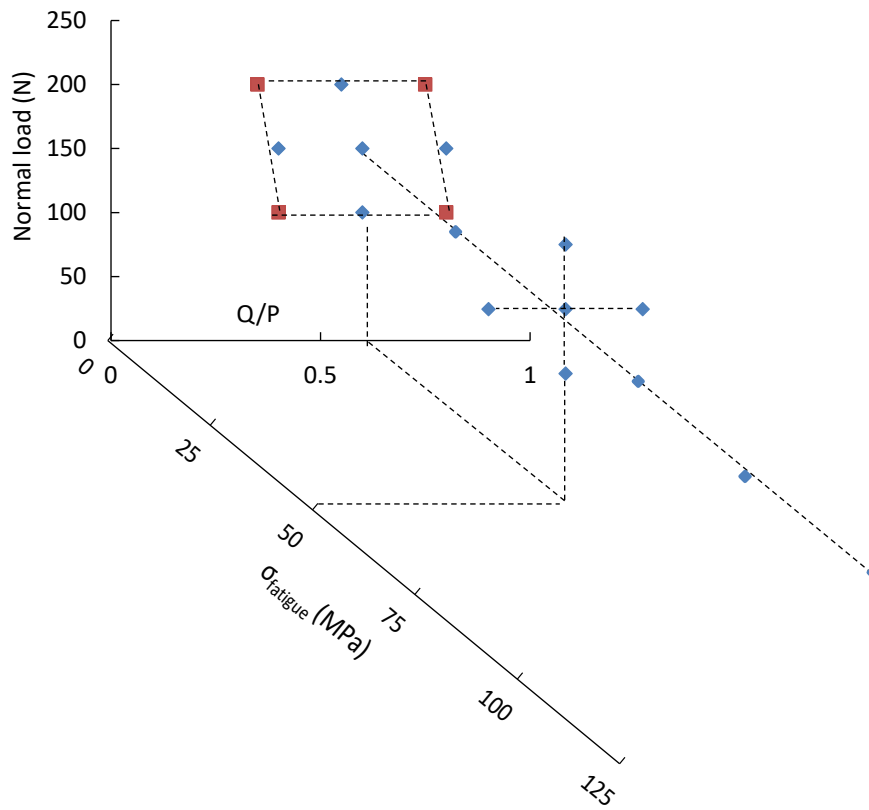


Figure 8: schematic representation of the test procedure as a function of the loading parameters: normal load, fatigue stress and Q/P ratio; square points correspond to the loading condition used for the identification of EP2 plastic law.

Table 4: test condition parameters under plain fretting and fretting fatigue conditions

associated symbol	P (N)	Q (N)	Q/P	σ fat (MPa)
Δ	100	40	0.4	0
Δ	100	60	0.6	0
Δ	100	80	0.8	0
\diamond	200	70	0.35	0
\diamond	200	110	0.55	0
\diamond	200	150	0.75	0
\square	150	60	0.4	0
\square	150	90	0.6	0
\square	150	120	0.8	0
\circ	150	60	0.4	50
\circ	150	120	0.8	50
\circ	200	120	0.6	50
\circ	100	60	0.6	50
+	150	90	0.6	25
+ \circ	150	90	0.6	50
+	150	90	0.6	75
+	150	90	0.6	100
+	150	90	0.6	125

4.2. Results

Figure 9 displays various fretting scars obtained for $P=200$ N as a function of the tangential force prescribed for the fretting conditions. Without tangential force (i.e. indentation) the surface damage is a small indent. With the increase of the tangential force, damage appears in the contact edges (darkest area). The higher the tangential force, the larger the sliding zone. These oxide debris are assumed to be related to the partial slip area where micro slidings are operating. Debris outer the contact side are also assumed to be related to debris ejection process from the sliding annulus.

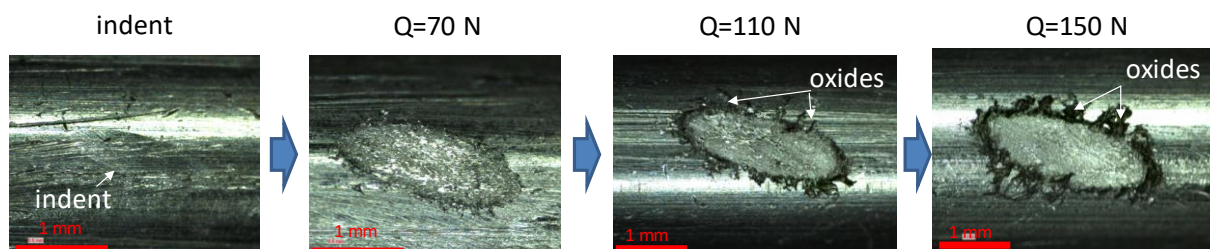


Figure 9: evolution of the contact interface as a function of the tangential force applied for a normal force of 200 N.

Figure 10 shows the evolution of the contact sizes (average value) as a function of the applied tangential force for all tested conditions, considering to an equivalent elliptical shape of the contact,

described in length and width by a_x and a_y respectively. The dimensions of the contact size were measured using binocular images taken in top view. The evolution of the contact size following fretting stresses appears to be nearly independent of the normal force and fatigue stress but highly influenced by the cyclic tangential force. Indeed, both contact width (a_y) and contact length (a_x) display a quasi-linear evolution versus the tangential force amplitude.

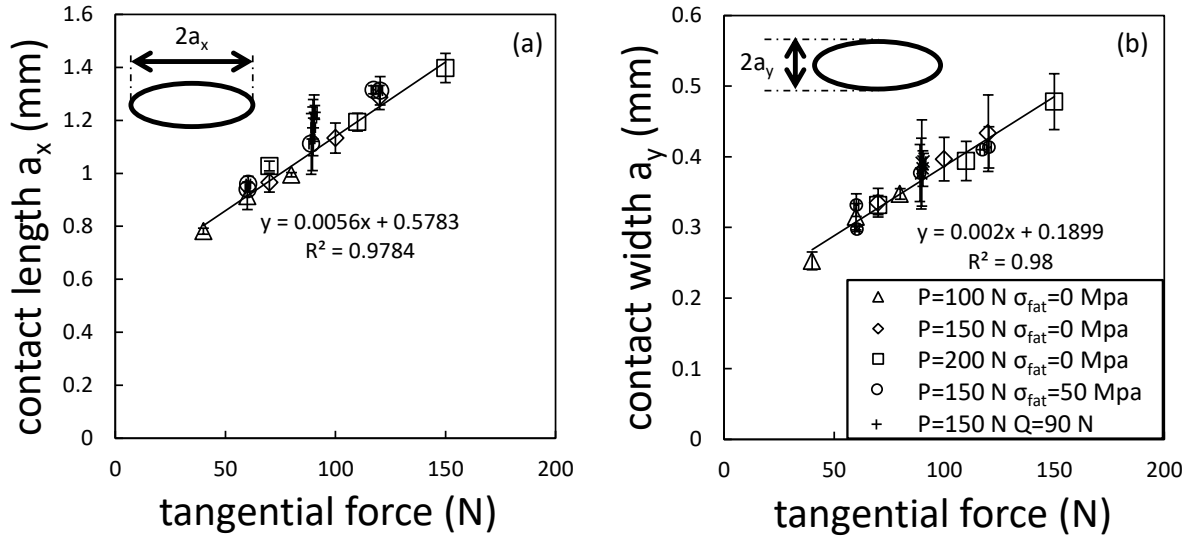


Figure 10: evolution of the length (a) and width (b), a_x and a_y , of the contact size as a function of the tangential force amplitude. The fit curve only considers the plain fretting experiments (i.e.

$\sigma_{max}=0$ MPa).

For technical applications, like expertise of overhead conductors, this result is very interesting. By measuring a_x and a_y from postmortem expertise of laboratory tests or real cable structures, the applied tangential force amplitude in the contact could be assessed. In a first approximation, considering only the plain fretting experiment, the tangential force amplitude can be assessed using the following equations:

$$a_x = a_{x,0} + K_{a,x} \times Q^* \rightarrow Q^* = \frac{a_x - a_{x,0}}{K_{a,x}} \quad (4)$$

$$\text{and } Q^* = \frac{a_y - a_{y,0}}{K_{a,y}} \quad (5)$$

With $a_{x,0}=0.56$ mm, $K_{a,x}= 0.57$ mm/N, $a_{y,0}=0.002$ mm and $K_{a,y}=0.19$ mm/N.

However, coupling between Q^* and P is occurring so that similar fretting scar dimensions could be observed for different (P, Q^*) loading couples as illustrated in fig. 11 a and b.

One alternative to dissociate P and Q^* consists in comparing the extension of the sliding zone (g) along the main axis X :

$$g_x = a_x - c_x \quad (6)$$

with a_x and c_x the contact radius and stick zone radius along the main axis x respectively (fig. 11 c).

Figure 11 d) plots the evolution of the ration g_x/a_x versus the Q^*/P fretting loading parameter so that:

$$\frac{g_x}{a_x} = f\left(\frac{Q^*}{P}\right) \quad (7)$$

Therefore, knowing Q^* from the linear expression eq. 4 induced from a_x , the corresponding P can be derived from g_x measurement and applying eq. 7 or through fig. 11 d).

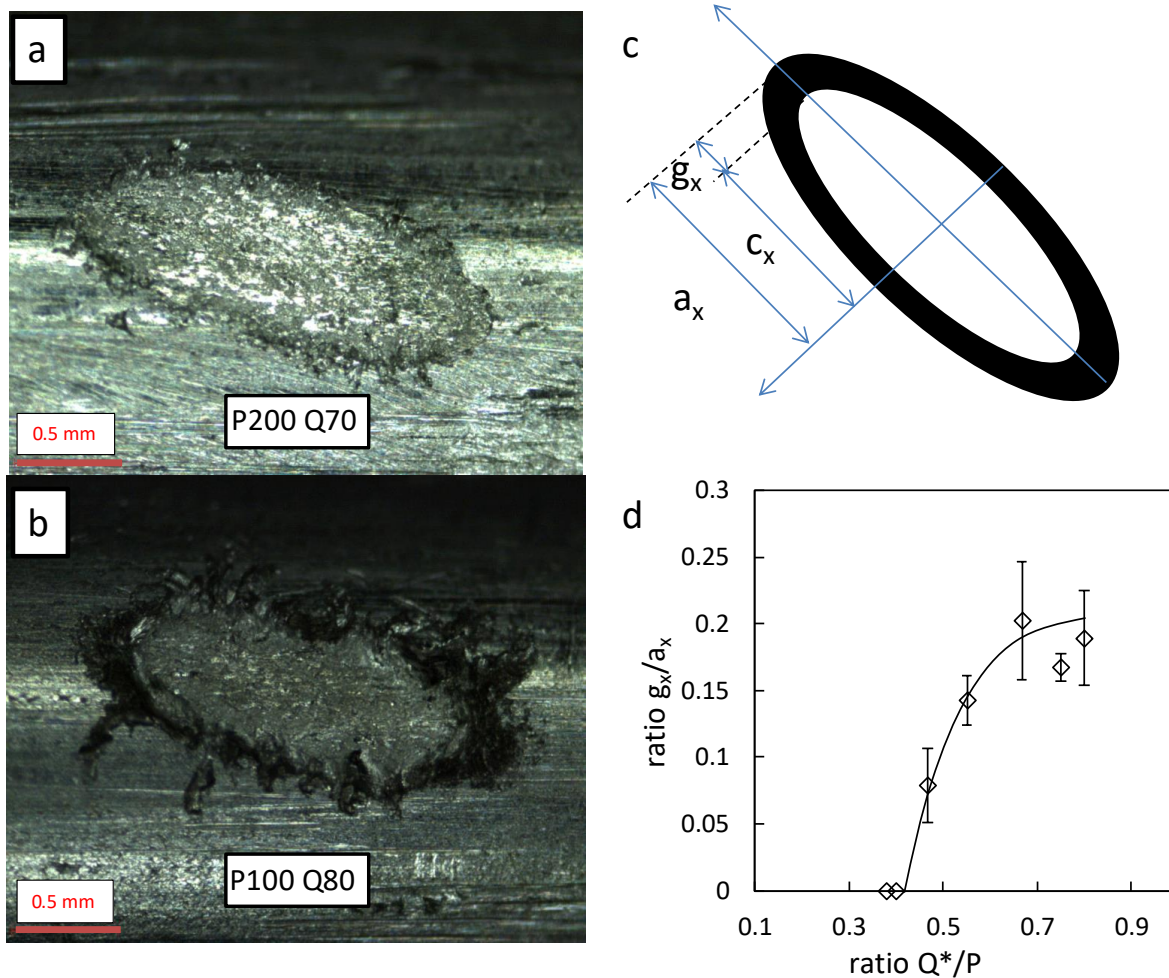


Figure 11: fretting contact trace for conditions a) P=100 N, Q=80 N and b) P=200 N, Q=70 N; c) illustration of the partial slip contact related identification of the partial slip contact parameter; d) evolution of g/a ratio versus Q^*/P ratio.

However, examining more precisely Figure 10, it can be noticed that a discrepancy occurs when significant fatigue stress is applied. This is confirmed by linear increase of a_x and a_y with σ_{max} for the given P= 150 N and Q=90 N fretting loading (fig. 12).

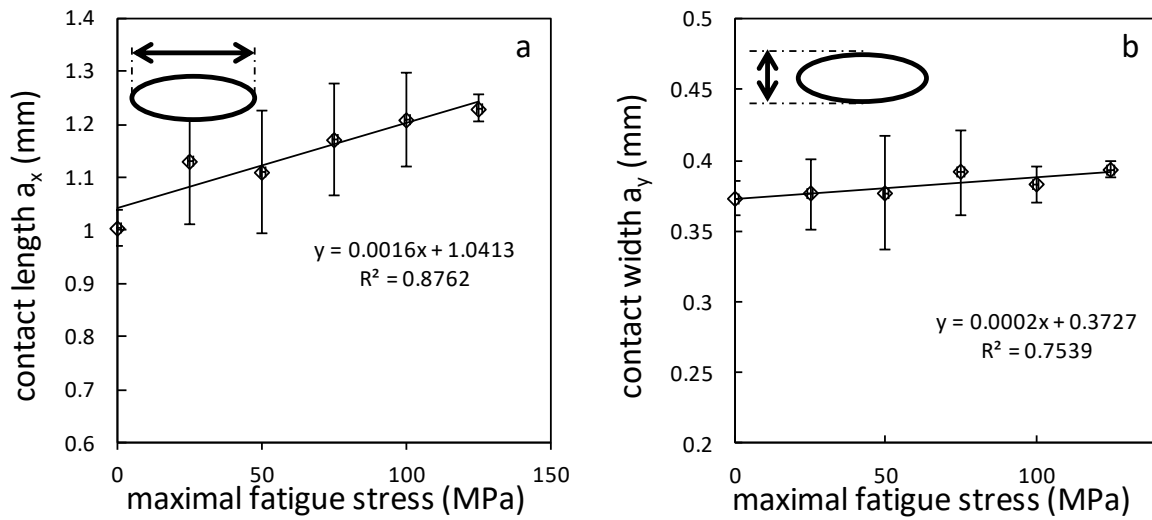


Figure 12: evolution of the contact length a_x (a) and width a_y (b) as a function of the fatigue stress for the condition $P=150$ N and $Q=90$ N.

The axial a_x extension seems more pronounced for the transverse a_y length. This can easily be justified by the fact that the tensile stress can generate a larger longitudinal extension of the plastic fretting scar. Hence if the (a_x, g_x) fretting scar expertise appears reliable to estimate both P and Q^* loading under plain fretting conditions, some caution must be considered when an additional fatigue stress is applied.

This experimental study allowed to highlight the linear relationship between the contact sizes a_x and a_y , and the amplitude of the tangential force applied in the contact for the studied domain. Thus, it is possible to assess the contact load (P, Q^*) of a cross-strand contact in a rope assembly from a single post-mortem examination of the fretting scar. From a technical and practical point of view this method is very interesting.

4.3. FE Model of fretting and fretting fatigue tests

To validate the EP1 plastic law, the experiments will be simulated using a FE model. Figure 13 shows the 3D Abaqus fretting model between the crossed wires contact using hybrid linear elements. These elements limit the computational time and are known to yield a reliable estimation of the hydrostatic

pressures generated by the contact. The length of the wire is 12 mm and the angle between the wires is set to 30° consistently with the testing configuration. Only a half wire is modeled to reduce the total number of elements. Thus, the model is composed of two half-wires made of a cylindrical surface in contact with each other and 3 flat surfaces. The boundary conditions applied to wire #2 consist in an embedding condition applied on its three flat faces. For wire #1, the three flat faces are used to apply the normal and tangential forces. The plastic law EP1 is considered for the simulations.

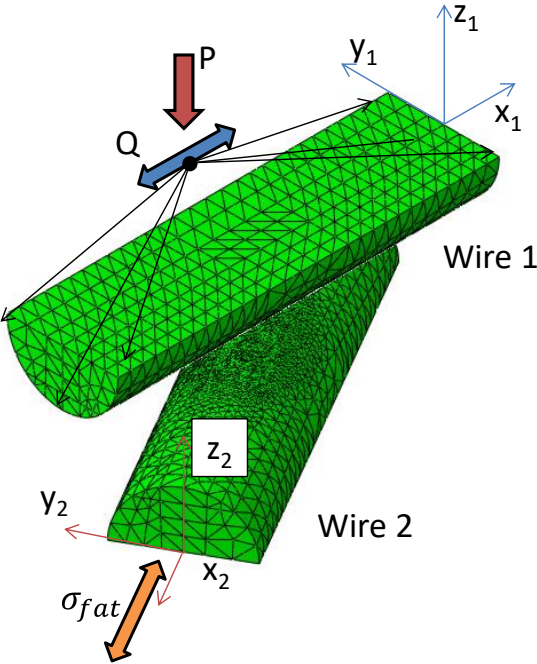


Figure 13: FE model for simulating the contact between 2 wires with 30° of orientation, the bullet point symbolizes the reference point where loading is applied

The criterion chosen to validate the plastic parameters is the modeled contact size which will be compared to the experimental test results. The former depends directly on the size of the mesh which is therefore very important for the simulations. A sensitivity analysis of the mesh size is achieved for 75, 50, 25 and 15 μm minimum size in the contact area. The tested condition corresponds to P=200 N, Q=150 N and 20 cycles with the plastic properties EP1 identified above. The results show good equivalence of stresses under contact for the 25 and 15 μm mesh sizes with

computation time of 10h30 and 30h respectively with 4 CPU. Thus, for the sake of calculation time, the size of 25 μm was kept in the sequel, presenting a good compromise between quality of the modeled contact size and associated computation time.

The model was decomposed into four steps of loading applied to the reference point driving the plane faces of wire #2:

Step 1 - applying the mean fatigue stress to the wire 2 (X2 loading)

Step 2 - Bringing into contact by moving wire 1 (Z displacement),

Step 3 - Application of the normal force for the contact (Z loading).

Step 4 - Application of the cyclic tangential force (on X1) and fatigue stress amplitude (on X2) during 20 cycles.

The simulation cannot accurately represent the tests performed and their experimental loading in terms of cycles: As a matter of fact, experiments were conducted with progressive loading until a targeted tangential force value was reached (table 4) and then 100 stabilized cycles were applied. In this configuration, too many cycles are required to simulate the contact. To save time, the experimental step corresponding to the progressive loading was ignored, and only 20 cycles are considered in the FE model. The following analysis Part 5.3. confirms that the steady state contact plastic extension is reached before 20 cycles. Then the assumption is made that equivalence is found between the experimental plastic stabilization after the progressive loading and the numerical plastic stabilization of the contact directly at the targeted tensile load, without considering the real plastic history in term of number of cycles.

Figure 14 compares the experimental and simulated contact sizes for width, a_y , length, a_x , and area, A. A rather good correlation is observed regarding the contact length a_x although a significant scatter is observed. Nevertheless, we observe that the evolution of the contact width as a function of the

tangential force does not follow the experimental one. The contact length is overestimated for the low tangential force values and underestimated for the high tangential force values. Besides, the contact widths provided by the model are largely underestimated with an average error of 18.5%. Regarding the contact area (i.e. $A=a_x a_y \pi$), large scatter is observed. The predicted areas are systematically underestimated; this infers that the contact plastic deformations are also underestimated which in turn suggests an over-estimation of the contact stress levels and cracking risk as well.

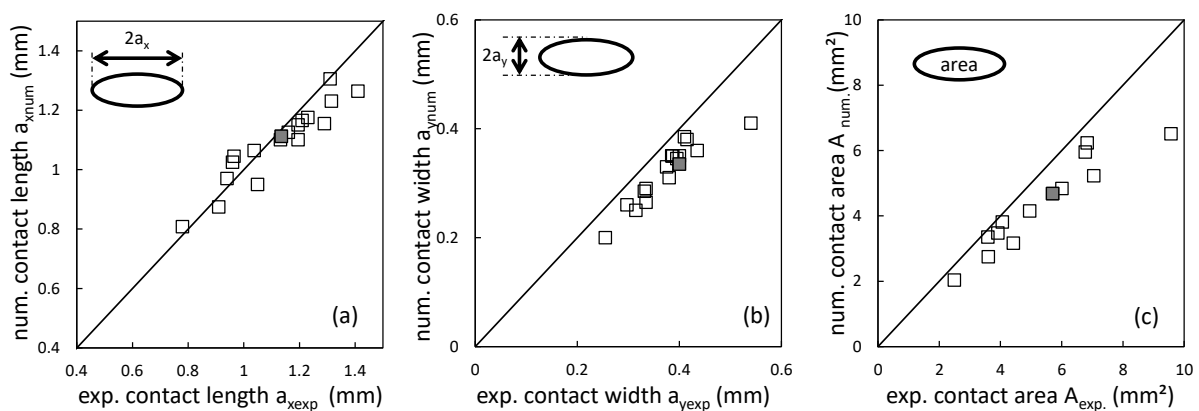


Figure 14: comparison between numerical and experimental length (a), width (b) and area (c) of the plastic contact size for all conditions (table 4); grey point is the fretting reference condition $P=150$ N $Q=90$ N.

The analysis of multiaxiality and proportionality allows to bring answers to the discrepancy between experimental and numerical results. Figure 15 shows the evolution of the minimum principal stress value, σ_3 , as a function of the maximum principal stress value, σ_1 , for the first and the 20th cycles and the evolution of the principal stresses for the 20th cycle at three locations around and in the contact. At the front of the contact principal stresses seems slightly out of phase (fig. 15 a) which is confirmed by the figure 15 (d) displaying a small hysteresis. The principal stress σ_2 goes from the minimum of the maximal principal stress to the maximum of the minimal principal stress. At the lateral edge, we observe a multiaxiality of the stress which seems to be an almost perfect proportionality (fig. 15 e) and the three principal stresses have a similar evolution (fig. 15 b). The stresses evolution is

significant and increases at the front while it decreases at the lateral edge. On the other hand, at the center of the contact, we observe a very non-proportional multiaxiality, cycling along an “eight” shape (fig. 15 f). The evolutions of the principal stress values σ_1 and σ_3 are similar but with an opposite sign, positive and negative respectively (fig.15 c). This trend is present at all points of the contact but the difference during the maximum and the minimum of the tangential force is more or less present depending on the analyzed location. It is worth noting that the initiation and propagation of cracks is strongly influenced by this type of multiaxial and non-proportional mechanical state, and this point is still an issue for modeling [23-25]. Moreover, the identification of the properties was carried out for uniaxial stress as well as for deformations not exceeding 1.1%. Thus, the stress state observed in the fretting tests presents a multiaxial state which is known to modify the evolution of the strain hardening [26-29].

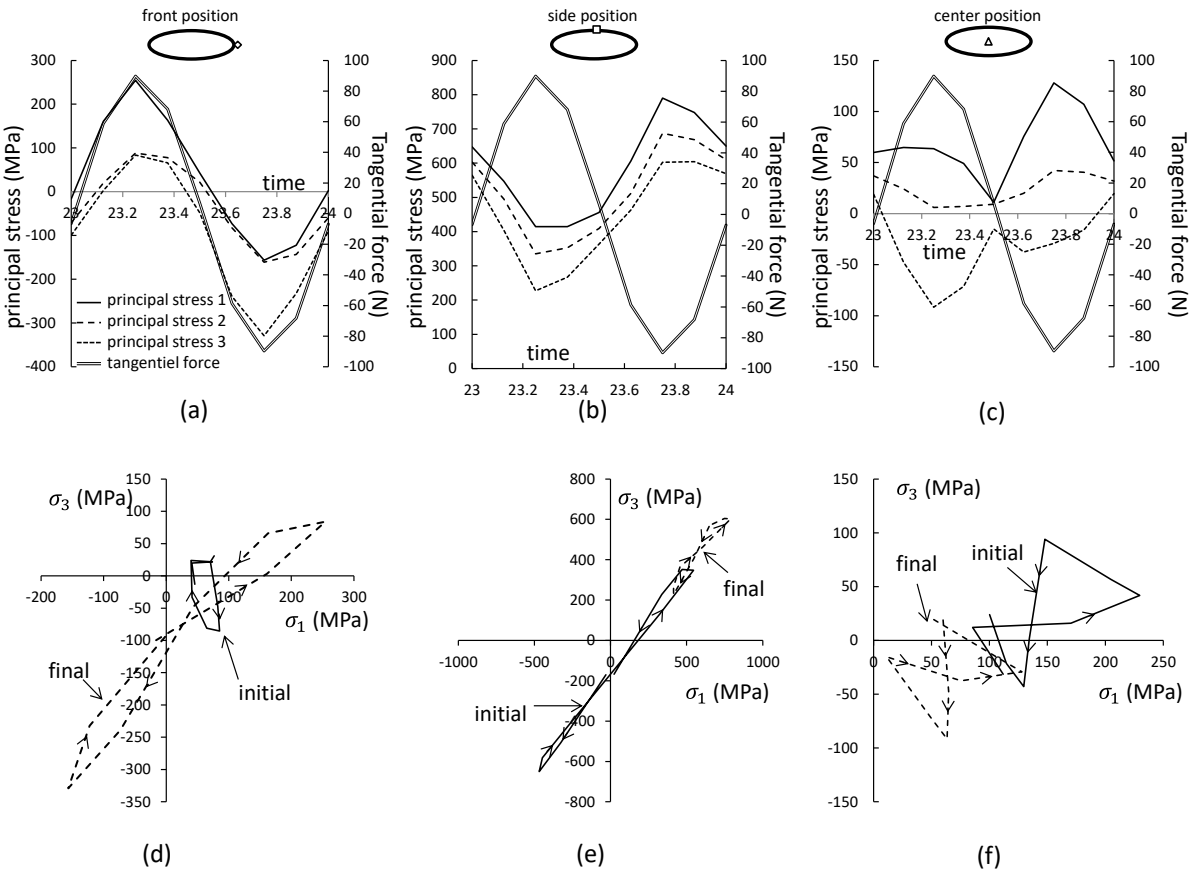


Figure 15: multiaxiality representation by plotting principal stresses as a function of time a) at the front of the contact b) at the contact lateral side and c) at the contact center for the fretting reference point $P=150$ N and $Q=90$ N; and plotting σ_3 as a function of σ_1 d) at the front of the contact e) at the contact lateral side and f) at the contact center for the fretting reference point $P=150$ N and $Q=90$ N.

From this analysis, it can be concluded that the EP1 plastic law, only estimated from tensile tests, does not offer a reliable estimation of the plastic properties for plastic contact stresses. As a matter of fact, it is well known that Chaboche's model well predicts ratcheting for uniaxial loading but consistently over predict ratcheting for multiaxial loading [26]. Then, two possibilities remain. The first one would be to enrich the model by using more complex models taking into account the multi-axiality and the non-proportionality [27-30]. However, the problem is that this kind of model requires a large number of parameters to be identified and subsequent more complex tests for their identification while we are limited by the geometry of our samples. A second solution consists in enriching the model identification by experimental condition more relevant with targeted use of the model. We have developed this option by adding fretting tests in the identification step.

4.4. Optimization of plastic parameters adding fretting tests (EP2)

In order to improve the prediction of plastic contact sizes in fretting and fretting fatigue, more information should be added in the optimization of plastic parameters. Thus, some fretting test results are combined with the tensile tests to optimize the plastic law.

Four plain fretting conditions representing the global contact loadings have been included in the plastic identification process: $P=100$ N $Q=40$ N, $P=100$ N $Q=80$ N, $P=200$ N $Q=70$ N and $P=200$ N $Q=150$ N.

The numerical strategy consists in considering as an initial input the EP1 plastic parameters derived from the tensile test analysis. Then a global L-M strategy combining simultaneously the tensile tests and the plastic contact sizes (a_x, a_y) of the four identification fretting tests is applied to extrapolate

through a reverse approach new EP2 plastic parameters. It was shown that using from the beginning a mesh size set to $h=25\ \mu\text{m}$ for fretting simulation leads to 10h30 computation times. To avoid a too long calculation time, a two-steps L-M strategy was applied: first, an EP2 law was derived using a coarse mesh size with $h=50\ \mu\text{m}$. Then, using the EP2 law a second set of simulations is achieved using a finer mesh size, $h=25\ \mu\text{m}$, to identify the final EP2 plastic law parameters.

Finally, the residue weights were balanced to obtain equal importance between the tensile tests containing 1066 points each and the fretting tests offering 8 points (4 widths and 4 lengths). While the weight of the residue in the tensile simulations is 1, the weight of the fretting simulations is 400.

For this convergence only 4 parameters were identified in order to save time during the optimization process. Thus, the parameter R_0 is set to 75 MPa, found from the first identification. The parameters deduced from this combined tensile and fretting scar size analysis (EP2) display a significant evolution to the previous optimizations (table 3). The isotropic plasticity shows a significant increase and is no longer negligible, the b parameter increasing from 1.5 to 13 MPa. The kinematic parameters also display a strong evolution which corresponds among other things to a balance to the evolution of the isotropic part.

Figure 16 compares the experimental and numerical EP2 contact sizes. A clear improvement is observed for the contact width a_y and length a_x and subsequent contact area assessment as compared to EP1 results in Figure 14. It is worth noting that only 4 of these 18 points were used for optimization. Besides, although the test conditions used for the optimization were under plain fretting, the fretting fatigue scar sizes are also very well modeled. The trend of contact length evolution and the underestimated values of the width as a function of tangential force are now corrected. Hence, the plastic parameters determined through this optimization process allow simulating the evolution of contact sizes under severe plastic deformation conditions and multiaxial problem in a relevant manner. It can be noticed that the contact width (a_y) for condition $P=200\ \text{N}$ and $Q=150\ \text{N}$ is difficult to assess; this value being out of the linear trend delineated by the other

points. Except for this point, the identification yields to a robust model, suggesting that the plastic parameters EP2 extracted from this dual cyclic tensile and cyclic plain fretting scar L-M optimization are very consistent to describe plain fretting but also fretting fatigue plastic contact extension.

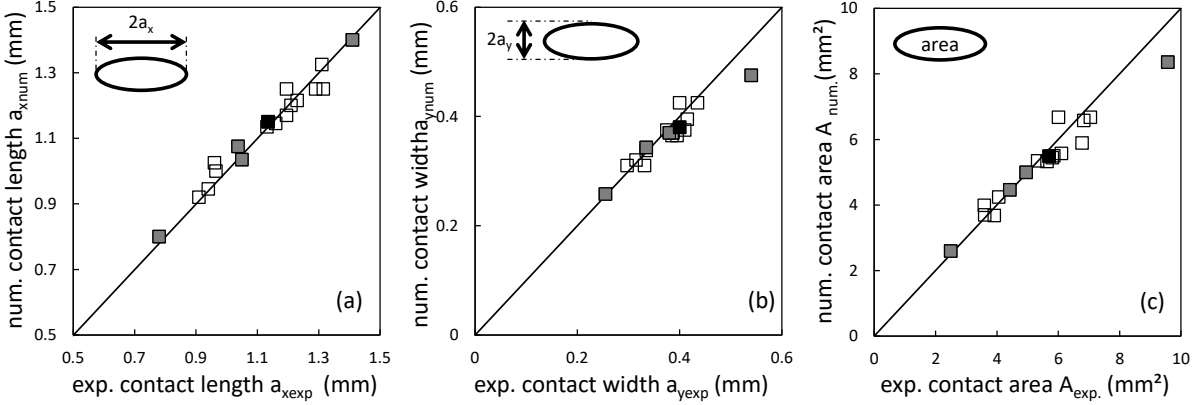


Figure 16: comparison between numerical EP2 and experimental length (a), width (b) and area (c) of the plastic extension of plain fretting and fretting fatigue scars (table 5); grey points correspond to the calibration tests; black point is fretting reference point P=150 N Q=90 N.

Figure 17 compares more precisely the EP2 predictions of the fretting fatigue contact scars varying the fatigue stress value σ_{max} . The contact length is well predicted but the contact width appears to be under-evaluated. The plastic contact length extension strongly depends on the fatigue strain. By contrast, the contact width can be affected by other plastic mechanism as described in [31], among which plastic extrusion phenomenon plays a crucial role, on the lateral sides of the contact by minoring the effect of the tensile strain effect.

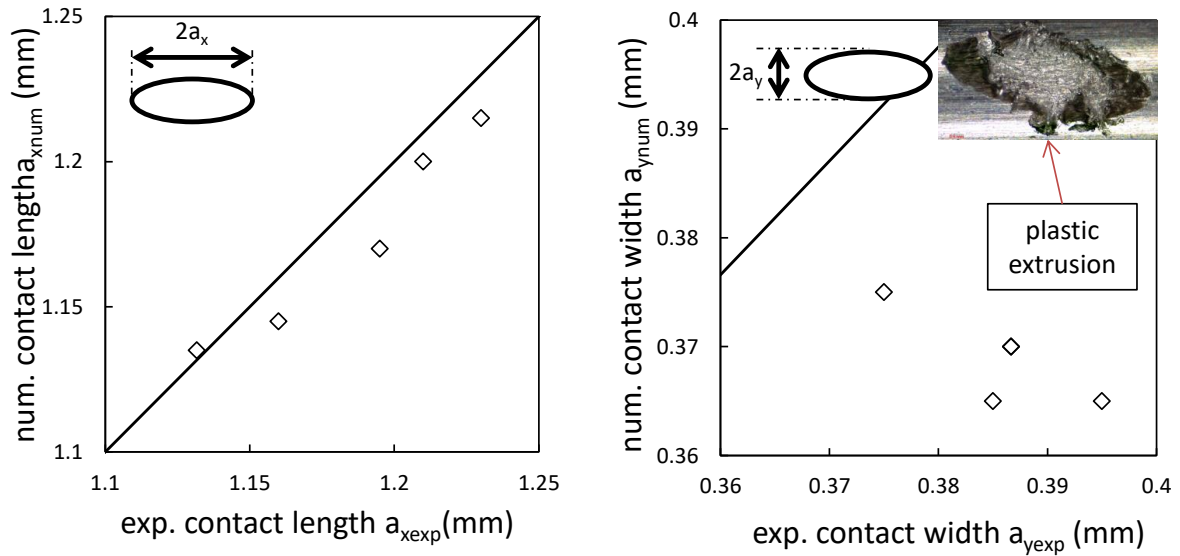


Figure 17: comparison between numerical and experimental length (a) and width (b) of the plastic contact size for fretting fatigue condition ($P=150$ N and $Q=90$ N, table 5).

5. Discussion

5.1. Optimization of plastic parameters adding simple indentation tests (EP3)

The given EP2 plastic law provides a rather good assessment of the plastic contact size extension. However, it requires a significant computational time equivalent to 1 week and half with 16 processors for identification (4 CPUS for 4 parallel fretting simulations). Thus, a study was carried out by only considering indentation tests. The normal forces included in the optimization are $P=50$, 100, 150 and 200 N. The model used is the same as presented above without the application of fatigue and/or tangential force steps and the mesh size is set to $25 \mu\text{m}$. Table 3 shows the optimized parameters deduced from this combined tensile and indentation plastic law identification method yielding the set of parameters EP3. These parameters are very close to the ones identified from the single tensile test analysis suggesting a clear improvement of contact size prediction. Figure 18 confirms this trend by comparing the fretting contact areas assessed from the given EP3 set of parameters versus experiments.

Like for EP1 set of parameters, a large scattering is observed. Therefore, even if the identification process is shortened by a factor 7 (2 days), compared to the former EP2, no clear improvement is observed in results. It can be concluded that to achieve reliable prediction of fretting fatigue, the elastoplastic identification needs to consider large strain which can be studied by cyclic fretting scar and cannot be approximated by only considering an indentation scar.

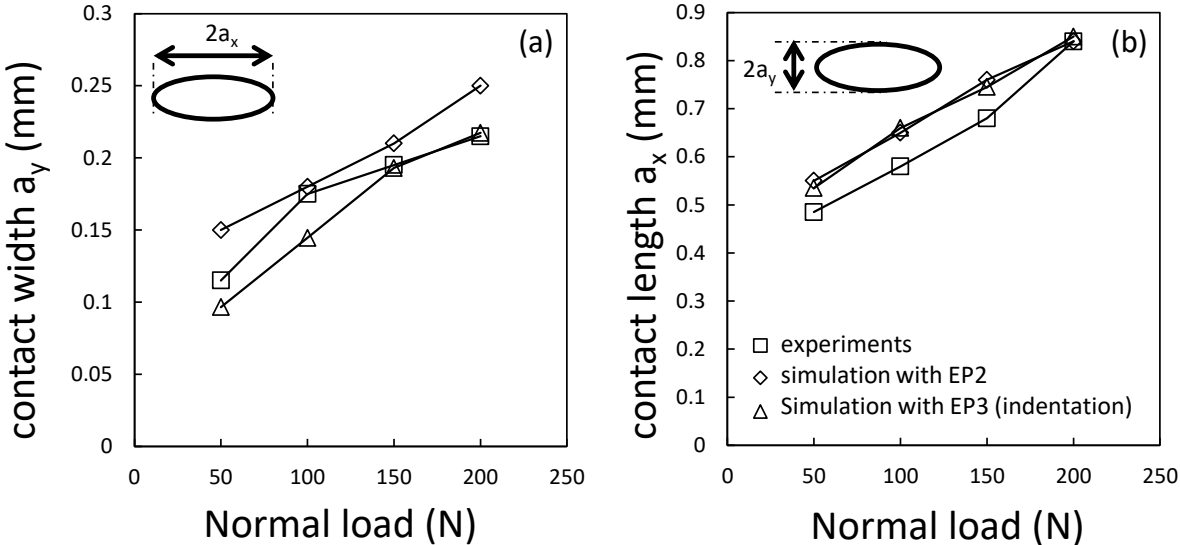


Figure 18: comparison of indentation length (a) and width (b) as a function of set of plastic parameter EP2 and EP3 used for non-linear hardening model versus experimental size

5.2. Sensitivity analysis as a function of the experimental dataset

Figure 19 illustrates the relative error between modeled and experimental values of contact size for both EP1 and EP2 set of parameters. The error corresponds to the average values of the ratio (model-exp)/exp for size prediction for the whole test series accounting for plane fretting and fretting fatigue tests achieved in this study. This analysis clearly underlines the better predictions reached by EP2 (optimization of plastic parameters adding fretting tests) corresponding to a coupled L-M analysis of cyclic tensile tests and only 4 selected plain fretting scars. This latter requires long and fastidious, plastic fretting simulations, the difficulties being mostly associated to slow FEA convergence. However, by considering two-step mesh size strategy described above (starting with a

coarse the a fine mesh), the identification of the EP2 parameters could be achieved in a reasonable CPU time (one week and half). Hence, if using the set of parameters EP1, the relative error of a_x , a_y and A (error=(num-exp)/exp) is above 7, 17 and 23% respectively. These latter are reduced to 2, 4 and 5% respectively when applying the EP2 set of parameters. It is worthy that the highest difference between the two plastic law identifications is observed for the contact area, which is the most important parameters to estimate reliable mean contact pressure and stress fields.

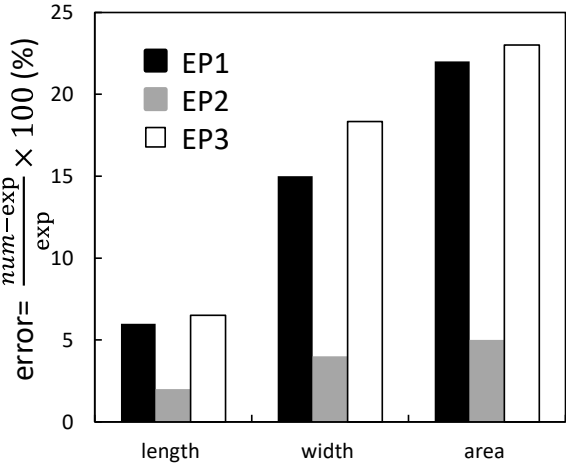


Figure 19: relative mean error of the contact size for the sets of plastic parameters EP1, EP2 and EP3 obtained by optimization for all experimental fretting conditions.

5.3. Plasticity through the contact

To further understand the contribution of fretting test in optimization process, let’s observe locally the mechanical stress state in the contact. At the edge of the contact in the longitudinal direction, the so-called front position in Figure 20 (a), the maximum loading corresponds to a cyclic tensile-compressive cycle, while at the lateral edge of the contact, the so-called side position in Figure 20(b), corresponds mainly to cyclic shearing. Finally at the center of the contact, the maximum strain values reached are in the direction of the fretting loading but with almost no cyclic loading (fig. 20 c). Strain values exceeds 3% irrespectively of the strain component, which is at least 3 times more than the tensile/compression tests. This point clarifies the limited quality of optimization of mechanical

behavior when only limited to tension/compression tests. On the other hand, the fretting tests display large plastic strain up to 5% for both compression and shear maximum values (figure 18). This justifies the better validity of the EP2 set of parameters obtained by the optimization based on the association of fretting and cyclic tensile tests.

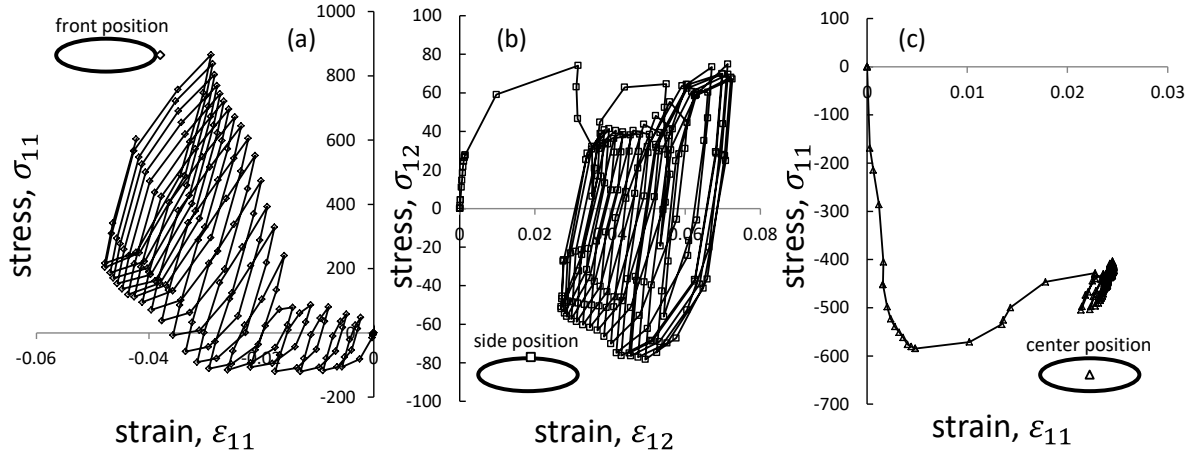


Figure 20: a) stress-strain evolution for the component 11 at the front location; b) stress-strain evolution for the component 12 at the side location; c) stress-strain evolution for the component 11 at the center location; test conditions $P=200$ N, $Q=150$ N at 20th cycle. Stress/strain components are chosen considering maximal values.

Another point of interest deals with the plastic stabilization. Figure 18 displays the stress-strain curves which tend to stabilize. To quantify this aspect an equivalent plastic deformation parameter is considered.

$$\varepsilon^{pl} = \sqrt{\frac{2}{3} \varepsilon_{ij}^{pl} \varepsilon_{ij}^{pl}} \quad (8)$$

The material response can evolve in three different behaviors: elastic shakedown associated to initial plastic deformation that stabilizes elastically after a certain number of cycles, the cyclic plasticity when a plastic deformation converges to a constant magnitude, and finally the ratcheting behavior which corresponds to a plastic deformation that is monotonically increasing with the loading cycles [32].

Figure 21 a) displays the evolution of the equivalent plastic strain at different point of the interface. Initially, a cyclic plastic deformation coupled with ratcheting is observed at the edge of the contact, front and side points. The ratcheting seems to slow down with the number of cycles until a quasi-stabilization, during the first 5 cycles, while cyclic plasticity is sustained and stable. It is worth noting that the strain amplitude is larger for the front point than for the side point, but the average strain value lower. It can be observed that at the center of the contact, a large ratcheting plasticity is operating and elastic shakedown seems not fully reached after 20th cycles.

Figure 21 b) shows the evolution of width and length of the contact as a function of the number of cycles. They evolve over the first 10 cycles, with the most important increase in the first cycle and stabilization after the 10th cycle. Hence, it can be concluded from this analysis that the increment of plastic deformation and related contact size extension becomes insignificant after 10 cycles. This justifies a posteriori the applied 20 numerical cycles to estimate the steady state plastic contact estimation in this numerical investigation.

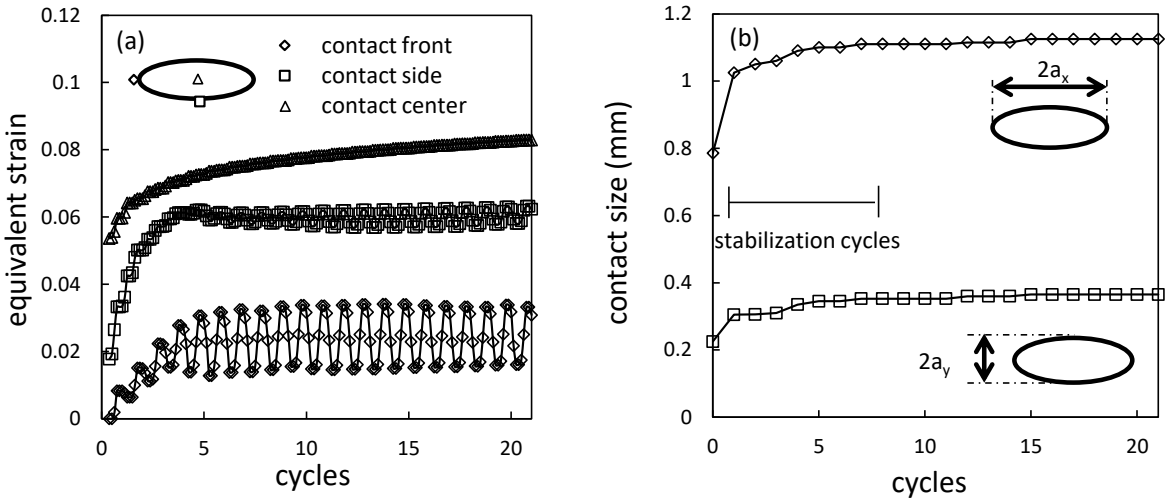


Figure 21: a) equivalent plastic strain at different position on the contact; b) width and length contact as a function of the fretting cycles.

5.4. Influence of the material behavior on crack nucleation criterion

A direct application of a reliable assessment of the plastic contact extension is a better estimation of the contact stress field and a more suitable evaluation of the cracking risk. To illustrate this aspect, the equivalent Smith Watson Topper (SWT) fatigue stress criterion is computed [33, 34]:

$$\sigma_{SWT} = \sqrt{E\gamma_{SWT}} \quad (9)$$

$$\gamma_{SWT}(M, \theta) = \sigma_{max}(M, \theta) \times \frac{\Delta\varepsilon(M, \theta)}{2} \quad (10)$$

With E the Young's modulus, M the studied point and θ the angle which describes the studied plane

$$\sigma_{max}(\theta, M) = \max_t[\sigma(t, \theta, M)] \quad (11)$$

$$\Delta\varepsilon(\theta, M) = \max_t[\varepsilon(t, \theta, M)] - \min_t[\varepsilon(t, \theta, M)] \quad (12)$$

Fig. 22 displays the distribution of the σ_{SWT} stress criterion for the reference condition P=150 N, Q=900 N fretting loading related to a fretting fatigue crack nucleation endurance at 10^7 cycles. This analysis compared the σ_{SWT} profiles assuming purely elastic behavior, and plastic hardening laws using EP1 and EP2 set of parameters. As expected, the elastic assumption leads to a discontinuous σ_{SWT} values at the contact edges loading to a non-realistic value of $\sigma_{SWT}=1100$ MPa at the hot spot (fig. 22 a). Severe stress gradients are observed along the contact length and along the Z subsurface axis at the vertical of the hot spot ($x=a_x$) contact edges. Hence, σ_{SWT} converges to zero at the edge of the stuck area ($x=c_x$) whereas it falls under 100 MPa below $z=0.2$ mm (fig. 22 b).

Plasticity laws in simulations extend significantly the contact area and proportionally reduce stresses. As expected, the softer EP2 plastic parameters induces a larger contact extension than other mechanical behavior: $a_{x,E} = 0.45$, $a_{x,EP1} = 0.95$ and $a_{x,EP2} = 1.1$ mm for elastic, EP1 and EP2 material behavior respectively. A proportional reduction of the maximum value of σ_{SWT} is also observed with $\sigma_{SWT,E} = 1100$ MPa, $\sigma_{SWT,EP1} = 650$ MPa and $\sigma_{SWT,EP2} = 500$ MPa respectively. Plastic simulations also reduce significantly the stress gradients. However, the elastoplastic σ_{SWT} values are still very high when compared to the plain fatigue limit $\sigma_{D-1} = 65$ MPa [8] in polycyclic condition. Moreover, this

condition is not supposed to initiate crack at 10^7 cycles. Considering elasticity, the stresses can reach very high values due to the linearity of the behavior. On the other hand, considering plasticity, the behavior yields to a large plastic zone with stresses well beyond the yield stress. The endurance limit value is reached at different depths, $l_{SWT,E}=0.19$ mm, $l_{SWT,EP1}=0.16$ mm and $l_{SWT,EP2}=0.14$ mm for elastic, EP1 and EP2 elastoplastic material behavior respectively. Hence, the softer elasto-plastic response the shorter the endurance limit distance is reached, at least for the studied interface. These results can be related to the non-local fatigue approach [35-38] consisting in computing the fatigue stress at optimal critical distance in order to capture the contact stress gradient effect and predict reliable cracking risks.

Note that the given simulation does not correspond to a fretting fatigue crack nucleation threshold condition so it cannot be considered for a post processing estimation of effective critical distance values like previously detailed in [39] for elastic contacts. However, it suggests that plastic accommodation can significantly modify such an estimation. It also underlines that it is essential to establish the most representative cyclic plastic law possible for fretting fatigue simulations. Hence the proposed plastic law identification approach, combining tensile tests and simple fretting tests, appears as a relevant strategy for future optimal critical distance calibrations.

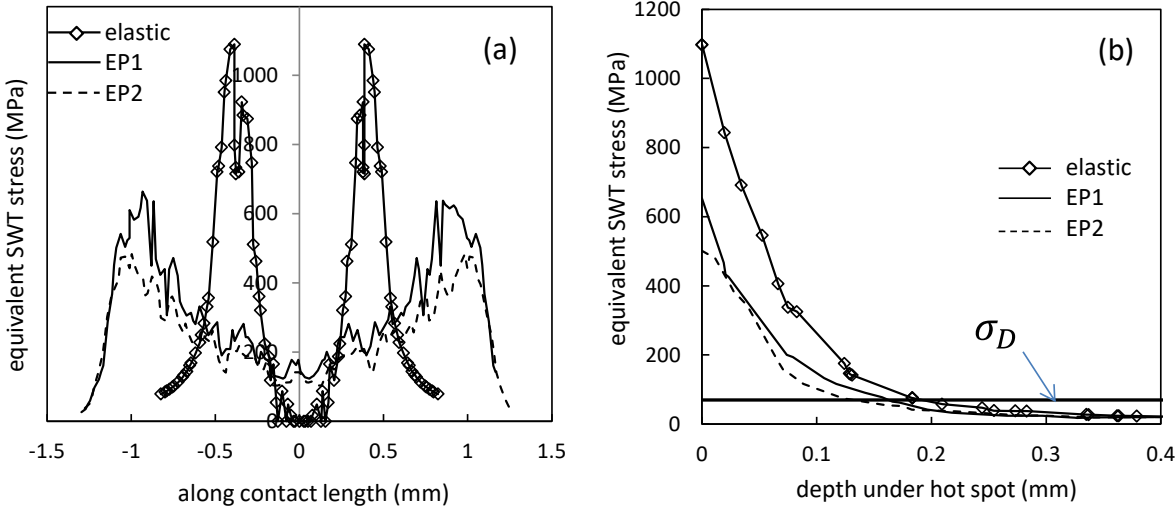


figure 22: evolution of the σ_{SWT} profiles for elastic, EP1 and EP2 plastic laws along X axis (a) and below the surface to the vertical of the $X=a_x$ contact borders (b) for P=150 N and Q=90 N.

6. Conclusion

The aim of this research work was to propose a method in order to achieve representative cyclic plastic properties of metallic materials for predicting the contact size extension under fretting fatigue loadings.

- Microstructural analysis showed that the studied aluminum wire displays a partially oriented $\langle 111 \rangle$ crystallographic direction collinear to the drawing process,
- The cyclic plastic law of the 1XXX aluminum wire was established applying a conventional cyclic tensile test procedure (EP1),
- Fretting and fretting fatigue tests have been performed to quantify the effect of the loading conditions regarding the plastic contact size extension. The analysis suggests that the contact size extension mainly depends on the applied tangential force amplitude rather than the normal force.
- The application of the EP1 cyclic plastic law does not provide relevant assessment of the experimental fretting and fretting fatigue contact sizes,
- A Levenberg-Marquardt algorithm was updated to include in the identification process the plastic model of a selected set of plain fretting scars. By including only 4 fretting tests in the optimization step, an optimized cyclic plastic law (EP2) have been identified providing better contact size predictions for all fretting and fretting fatigue tests,
- If the identification process is limited to simple indentation tests (EP3), the prediction of the fretting and fretting fatigue plastic contact sizes is not improved,
- A numerical investigation confirms that the mechanical state of fretting contacts is fully multiaxial, with compressive hydrostatic stresses and corresponds to higher strain level than usual imposed using uniaxial tests. This explains why the EP2 strategy is better than the conventional EP1

methodology: the specificity of the fretting loading need to be included in the plastic law identification.

Acknowledgements

The authors fully acknowledge Jean-Christophe Teissedre and Djamel Missoum Benziane at Centre des Matériaux (Mines Paris – PSL) for their help in mechanical testing and model optimization methods respectively.

References

- [1] R.B. Kalombo, J.A. Araújo, J.L.A. Ferreira, C.R.M. da Silva, R. Alencar, A.R. Capra, Assessment of the fatigue failure of an all aluminum alloy cable (AAAC) for a 230 kV transmission line in the Center-West of Brazil. *Eng Fail Anal* 2016, 2012, 77–87.
- [2] S. Lalonde, R. Guilbault, S. Langlois. Numerical analysis of ACSR conductor-clamp systems undergoing wind-induced cyclic loads. *IEEE Trans. Power Deliv* 33, 2018, 1518–26
- [3] J. Said, S. Garcin, S. Fouvry, G. Cailletaud, C. Yang, F. Hafid, A multi-scale strategy to predict fretting-fatigue endurance of overhead conductors. *Tribol Int* 143, 2020, 106053.
- [4] R.B. Waterhouse *Fretting fatigue*. AppliedScience Publishers; 1981.
- [5] J.J. Madge, S.B. Leen, I.R. McColl, P.H. Shipway, Contact-evolution based prediction of fretting fatigue life: effect of slip amplitude, *Wear* 262, 2007, 1159-1170
- [6] P. Arnaud, S. Fouvry, Modeling the fretting fatigue endurance from partial to gross slip: The effect of debris layer, *Tribology International* 143, 2020, 106069
- [7] P. Arnaud, S. Baydoun, S. Fouvry, Modeling adhesive and abrasive wear phenomena in fretting interfaces: A multiphysics approach coupling friction energy, third body and contact oxygenation concepts, *Tribology International* 161, 2021, 107077
- [8] A. Warmuth, S. Pearson, P. Shipway, W. Sun. The effect of contact geometry on fretting wear rates and mechanisms for a high strength steel. *Wear* 301, 2013, 491–500
- [9] C.F.B. Sandoval, L. Malcher, F.A. Canut, L.M. Araújo, T.C.R. Doca, J.A. Araújo, Micromechanical Gurson-based continuum damage under the context of fretting fatigue: Influence of the plastic strain field, *international Journal of Platicity* 125, 2020, 235-264.
- [10] J.M. Ambrico, M.R. Begley , Plasticity in fretting contact, *journal of the Mechanics and Physics of Solids* 48, 2000, 2391–2417
- [11] J.M. Ambrico, M.R. Begley The role of macroscopic plastic deformation in fretting fatigue life predictions *International Journal of Fatigue* 23, 2001, 121-128

- [12] F. Lu, J. Xu Evaluation of cyclic inelastic response in fretting based on unified Chaboche model International Journal of Fatigue 27, 2005, 1062–1075
- [13] V. Zolotarevskiy, Y. Kligerman, I. Etsion Elastic–plastic spherical contact under cyclic tangential loading in pre-sliding Wear 270, 2011, 888–89
- [14] M. Alquezar, V. Arrieta, A. Constantinescu, L. Flandi, M. H. Maitournam, P. Wackers Laboratoire Computational fretting fatigue maps for different plasticity models Fatigue Fract Engng Mater Struct 37, 2014, 446–461
- [15] K. Anderson, J. Weritz, J. Gilbert Kaufma, ASM Handbook, Volume 2B, Properties and Selection of Aluminum Alloys, DOI 10.31399/asm.hb.v02b.a0006552
- [16] P. Koprowski, M. Lech-Grega, Ł. Wodziński, B. Augustyn, S. Boczka, M. Ożóg b, P. Uliasz, J. Żelechowski, W. Szymański, The effect of low content additives on strength, resistivity and microstructural changes in wire drawing of 1xxx series aluminum alloys for electrical purposes, Materials Today Communications 24, 2020, 101039
- [17] P. Koprowski, M. Bieda, S. Boczka, A. Jarzębska, P. Ostachowski, J. Kawałko, T. Czeppe, W. Maziarz, M. Łagoda, K. Sztwiertnia, AA6013 aluminum alloy deformed by forward-backward rotating die (KoBo): Microstructure and mechanical properties control by changing the die oscillation frequency, J. Mater. Process. Technol. 253, 2018, 34–42
- [18] P. Koprowski, M. Bieda, S. Boczka, A. Jarzębska, P. Ostachowski, J. Kawałko, T. Czeppe, W. Maziarz, M. Łagoda, K. Sztwiertnia, AA6013 aluminum alloy deformed by forward-backward rotating die (KoBo): microstructure and mechanical properties control by changing the die oscillation frequency, J. Mater. Process. Technol. 253, 2018, 34–42
- [19] X. Ma, J. Chen, Y. Yang, L. Li, Z. Chen, W. Yan, Temperature dependence of microstructure and texture in cold drawn aluminum wire, Trans. Nonferrous Met. Soc. China 27, 2017, 763–770
- [20] J. Besson, G. Cailletaud, J.L. Chaboche, S. Forest, Mécanique non linéaire des matériaux, 2001
- [21] Zset software <http://www.zset-software.com/>
- [22] K. Levenberg, A Method for the Solution of Certain Non-Linear Problems in Least Squares, Quarterly of Applied Mathematics 2, 1944, 164–168.
- [23] T. Bonniot, V. Doquet, S. H. Mai. Mixed mode II and III fatigue crack growth in a rail steel. Int J Fatigue 115, 2018, 42–52.
- [24] T. Bonniot, V. Doquet, S. H. Mai, Fatigue crack growth under non-proportional mixed-mode I + II. Role of compression while shearing, International Journal of Fatigue 134, 2020, 105513
- [25] M. Akama, A. Kiuchi, Long co-planar mode III fatigue crack growth under nonproportional mixed mode loading in rail steel. J rail and rapid transit 226, 2012, 489–500.
- [26] S. Bari, T. Hassan, An advancement in cyclic plasticity modeling for multiaxial ratcheting simulation, International Journal of Plasticity 18, 2002, 873–894

- [27] T. Hassan, S. Kyriakides Ratcheting of cyclically hardening and softening materials, part II: multiaxial behavior. *Int. J. Plasticity* 10, 1994, 185–212.
- [28] McDowell, D.L.,. Stress state dependence of cyclic ratcheting behavior of two rail steels. *Int. J. Plasticity* 11, 1995, 397–421.
- [29] G. Z. Voyiadjis, I. N. Basuroychowdhury, A plasticity model for multiaxial cyclic loading and ratchetting, *Acta Mechanica* 126,1998, 19-35
- [30] R. Döring, J. Hoffmeyer, T. Seeger, M. Vormwald, A plasticity model for calculating stress–strain sequences under multiaxial nonproportional cyclic loading, *Computational Materials Science* 28, 2003, 587–596
- [31] T. Akaki, K. Kato, Plastic flow process of surface layers in flow wear under boundary lubrication, *Wear* 117, 1987, 179-196
- [32] M.R. Begley, J.W. Hutchinson, Plasticity in fretting of coated substrates. *Engineering Fracture and Mechanics* 62, 1999, 145–164.
- [33] K.N. Smith, P. Watson, T.H. Topper, A stress-strain function for the fatigue of metals, *J Mater* 5 (4), 1970, 767–778.
- [34] D. Scocie, Multiaxial fatigue damage models, *Journal of Engineering Materials and Technology* 109,1987, 293-298
- [35] I.V. Papadopoulos, Invariant formulation of a gradient dependent multiaxial high-cycle fatigue criterion, *Engineering Fracture Mechanics* 55, 1996, 513–528.
- [36] S. Fouvry, P. Kapsa, F. Sidoroff, L. Vincent. Identification of the characteristic length scale for fatigue cracking in fretting contacts. *J. Phys. IV JP* 8, 1998, 2–9.
- [37] J.A. Araújo, L. Susmel, D. Taylor, J.C.T. Ferro, J.L.A. Ferreira. On the prediction of high- cycle fretting fatigue strength: theory of critical distances vs. hot-spot approach. *Eng Fract Mech* 75, 2008, 1763–78.
- [38] D. Taylor, The theory of critical distances. *Eng Fract Mech* 75, 2008, 1696–705.
- [39] S. Fouvry, H. Gallien, B. Berthel, From uni- to multi-axial fretting-fatigue crack prediction: development of a stress-gradient-dependent critical distance approach, *International Journal of Fatigue* 62, 2014, 194–209